PHYSICAL REVIEW B **86**, 184203 (2012)

# Alloy microstructures with atomic size effects: A Monte Carlo study under the lattice statics formalism

Céline Varvenne,[*] Alphonse Finel, Yann Le Bouar, and Mathieu Fèvre
*Laboratoire d'Etude des Microstructures, ONERA-CNRS, BP72, 29, Avenue de la Division Leclerc, 92322 Châtillon Cedex, France*

(Received 26 July 2012; published 26 November 2012)

We present in this paper atomic scale Monte Carlo simulations of microstructure evolutions in the presence of atomic size mismatch, performed on a rigid lattice. The lattice statics formalism is used to obtain effective pair interactions (EPIs) from a continuous empirical description of alloy energetics that includes elastic relaxations in the harmonic approximation. These EPIs are long-ranged and are introduced in a Monte Carlo scheme to compute alloy properties. The influence of atomic size mismatch on EPIs as well as on microstructure evolutions is investigated in the case of a model binary fcc alloy. The microstructure evolution with atomic size mismatch operates mainly by shape changes and by the development of spatial correlations between precipitates. Our aim is also to provide a method to include elastic effects at the atomic scale starting from material macroscopic data, without any requirement of realistic continuous interatomic potential calibration. A commonly found approach in microscopic mean-field simulations is to use, at the atomic scale, effective elastic interactions inherited from continuum linear elasticity. We derive here a different and original method: the discrete lattice approach (DLA) that both converges to the continuum theory of elasticity (long-range aspect) and takes into account the discreteness of the lattice. It allows us to correctly reproduce the whole range of elastic interactions, down to the atomic scale, successfully improving the simple use of continuum elasticity, without the prior knowledge of any interatomic potential. Finally, the accuracy of the DLA is quantitatively verified through a detailed comparison between the microstructural evolutions obtained with this approach and the original lattice statics approach.

DOI: 10.1103/PhysRevB.86.184203 PACS number(s): 61.72.−y, 64.70.kd, 07.05.Tp, 46.25.−y

## I. INTRODUCTION

Macroscopic properties of metallic alloys are strongly related to the spatial organization of the different stable phases. When atomic radii of the alloy components differ, particular coherent microstructure morphologies are found, such as specific shapes and spatial alignments of precipitates. This atomic size effect is responsible for coherency stress that induces long-range elastic interactions. In the scope of a good understanding of microstructure formation, particular attention has to be paid to the role of these elastic effects.

Mesoscopic scale studies, using continuum theory of elasticity[1] coupled with continuous methods (such as phase field) have been successfully applied to explain elasticity related physical problems. One can mention, without being exhaustive, the directional coarsening phenomenon,[2] chessboard-like microstructure formation[3] or cuboidal precipitates that form ordered arrays.[2] However, this continuous description suffers from important limitations at small scale when effects due to the discreteness of the underlying lattice cannot be ignored. Indeed, interfaces are diffuse in phase field methods, whereas in most experimental situations, sharp interfaces are observed. Early stages of precipitation cannot be reached either, because subcritical fluctuations as well as critical nucleus often involve very small length scales. An atomic scale treatment of elasticity is then required for a correct description of such phenomena.

The lattice statics formalism[4,5] (LS), which consists namely in relaxing the elastic degrees of freedom within a rigid lattice framework, leads to an approach where the time scale is only controlled by atomic jumps. Approaches that deal with similar working hypothesis can be found in the literature.[6] This point is of great interest since the characteristic time scale becomes the diffusion time scale. By combining the LS formalism with Monte Carlo simulations, large systems (several millions of atoms) can therefore be simulated; microstructure formations, partly driven by coherent elasticity, are then accessible at the atomic scale.

In this work, after a brief presentation of the LS formalism, we calculate elastic interactions for a model binary fcc alloy exhibiting a miscibility gap at low temperature. This very simple system highlights the main features of elastic discrete interactions. Special attention is then devoted to the long-wavelength limit of the LS and its link with continuum linear elasticity. We then discuss two different techniques to calibrate discrete elastic interactions on macroscopic quantities. In particular, we propose a method that determines coherency-induced elastic interactions using the single knowledge of a few macroscopic quantities, namely, elastic constants and stress-free eigenstrain. We show that this approach leads to elastic interactions very similar to the ones derived within the LS formalism, down to the atomic scale, but with the important advantage that the implementation of the method does not require the preliminary knowledge of a continuous interatomic potential.

Finally, microstructure calculations are performed. We investigate the influence of atomic size mismatch on microstructure morphology at the atomic scale and compare the different treatments of discrete elasticity on microstructure simulations.

## II. ATOMIC TREATMENT OF ELASTICITY

### A. Lattice statics approach

We consider a binary (A-B) alloy, where $\bar{c}$ is the average concentration in B atoms, and with a Bravais lattice with one atom per cell. The alloy energy $E(\{\mathbf{R_n},\mathbf{c_n}\})$ can be written as a function of the atomic positions $\mathbf{R_n}$ and the occupation site variables $c_n$ ($c_n = 1$ if there is a B atom at $\mathbf{R_n}$ and 0 otherwise). In the case of a small atomic size effect, the microstructure stays coherent and it is relevant to define a homogeneous reference state around which internal energy can be expanded to a limited range.

This state can be chosen in a number of ways;[7] a convenient one is a homogeneous solid solution with $c_n = \bar{c}$ at each site $n$ and with a lattice parameter which minimizes the total energy $E(\{\mathbf{R_n},\bar{\mathbf{c}}\})$.

The lattice statics analysis is based on a second-order expansion of the total energy around this reference state. This requires an identification of small quantities such as concentration variations $\delta c_n = c_n - \bar{c}$, displacements $\delta\mathbf{u_n}$, and average strain $\bar{\epsilon}_{ij}$. These latter terms correspond to the development of the total atomic displacements $\mathbf{u_n}$ in the following form:

$$u_n^i = \bar{\epsilon}_{ij} R_n^{0j} + \delta u_n^i, \tag{1}$$

where $\mathbf{R_n^0}$ are the atomic positions in the reference state and the total displacements $\mathbf{u_n} = \mathbf{R_n} - \mathbf{R_n^0}$ are expressed with respect to the reference state. Sums over repeated Cartesian indices are implicit. If we neglect the vibrational component of the equilibrium state, the lattice statics analysis consists in imposing mechanical equilibrium on $\delta\mathbf{u_n}$. To do so, and without lost of generality concerning the identification of the role of $\delta\mathbf{u_n}$, we may impose $\bar{\epsilon}_{ij} = 0$ (i.e., $\mathbf{u_n} = \mathbf{0}$ at the boundaries of the system, or periodic boundary conditions on $\mathbf{u_n}$) and $\sum_n \delta c_n = 0$. This makes the first-order terms vanish in the expansion. When limited to the second order, the energy becomes

$$\begin{aligned} E_{\mathrm{LS}} = E_0 + \frac{1}{2}\sum_{n,m}\big[&\theta_{nm}\delta c_n \delta c_m + 2\psi_{mn}^i \delta c_n \delta u_m^i \\ &+ \phi_{nm}^{ij}\delta u_n^i \delta u_m^j\big], \end{aligned} \tag{2}$$

where $E_0$ is the reference state energy. The chemical interactions $\theta_{nm}$, the components $\psi_{nm}^i$ of the Kanzaki forces, and the force-constant matrix $\phi_{nm}^{ij}$ are defined by

$$\begin{aligned} \theta_{nm} &= \left.\frac{\partial^2 E}{\partial c_n \partial c_m}\right|_{\mathbf{R_0},\bar{\mathbf{c}}}, \quad \psi_{nm}^i = \left.\frac{\partial^2 E}{\partial u_n^i \partial c_m}\right|_{\mathbf{R_0},\bar{\mathbf{c}}}, \\ \phi_{nm}^{ij} &= \left.\frac{\partial^2 E}{\partial u_n^i \partial u_m^j}\right|_{\mathbf{R_0},\bar{\mathbf{c}}}. \end{aligned} \tag{3}$$

Note that derivatives with respect to $\delta c_n$ and $\delta u_n^i$ are identical to those with respect to $c_n$ and $u_n^i$, respectively. Besides, because of the symmetry properties of the lattice, the second derivatives obey the following rules:

$$\begin{aligned} \theta_{nm} &= \theta_{mn}, \quad \psi_{mn}^i = -\,\psi_{nm}^i, \\ \phi_{nm}^{ij} &= \phi_{mn}^{ij} = \phi_{mn}^{ji}, \\ \sum_m \phi_{nm}^{ij} &= 0, \quad \sum_m \psi_{mn}^i = 0. \end{aligned} \tag{4}$$

The system is supposed to be at the local elastic equilibrium, which is justified in the context of diffusive solid-state transformations. Static displacements are then obtained by solving the set of equations $\frac{\partial E}{\partial u_n^i} = 0$. Using periodic boundary conditions, the resolution leads to

$$u^i(\mathbf{q}) = -\,(\phi^{-1})^{ij*}(\mathbf{q})\,\psi^j(\mathbf{q})\delta c(\mathbf{q})\,, \quad \forall \mathbf{q} \neq 0, \tag{5}$$

where $f^*(\mathbf{q})$ is the complex conjugate of $f(\mathbf{q})$ and the Fourier transforms are defined by

$$f(\mathbf{q}) = \sum_n f_n\, e^{-i\mathbf{q}\cdot\mathbf{R_n}}. \tag{6}$$

The $\mathbf{q}$ vector is limited to the first Brillouin zone of the structure. The static displacements are then inserted into Eq. (2) and an Ising-like expression is obtained for the energy:

$$\begin{aligned} E &= E_0 + \frac{1}{2N}\sum_{\mathbf{q}\neq 0} V(\mathbf{q})|\delta c(\mathbf{q})|^2 \\ &= E_0 + \frac{1}{2}\sum_{n,m} V_{nm}\delta c_n \delta c_m, \end{aligned} \tag{7}$$

where $N$ is the number of atoms. The $V_{nm}$ terms are called effective pair interactions (EPIs). Their Fourier transform $V(\mathbf{q})$ contains two distinct contributions:

$$V(\mathbf{q}) \;=\; \theta(\mathbf{q}) \,+\, J(\mathbf{q}), \tag{8}$$

where $\theta(\mathbf{q})$ is the Fourier transform of the chemical interactions $\theta_{nm}$ given in Eq. (3) and where $J(\mathbf{q})$, the Fourier transform of the strain-induced pair interactions $J_{nm}$, is given by

$$J(\mathbf{q}) = -\psi^i(\mathbf{q})\,(\phi^{-1})^{ij}(\mathbf{q})\,\psi^{j*}(\mathbf{q}). \tag{9}$$

$J(\mathbf{q})$ differs from zero only if there is an atomic size effect between the alloy components.

The main interest of the lattice statics formalism is that, within this approach, the alloy energy is only a function of compositional variables. Extensions to multicomponent alloys,[8] to lattices with several atoms per unit cell,[9] and to interstitial solid solutions[1] are straightforward in principle. An important outcome of this method is to provide an energetic model to compute alloy properties within efficient discrete statistical tools (Monte Carlo methods, mean-field approximation,...). Free energy contribution due to deviations around the lattice Statics equilibrium could be incorporated within the quasiharmonic approach.[7]

### B. Effective pair interactions

Lattice statics method implementation requires the computation of the various second derivatives of a given continuous interatomic potential, parametrized on a specific alloy. Details of the implementation within the context of pair potentials,[7,10] the embedded atom method (EAM),[7,11] and all-electron methods[12] are given in the literature.

As explained in the Introduction, one of the aims of our paper is to analyze the major trends of atomic size mismatch on microstructural evolutions at the atomic scale. Therefore, for the sake of simplicity, we have chosen a Lennard-Jones potential to simulate a phase segregation, which is very flexible in comparison with more realistic potentials in terms of control of the competition between chemical and elastic effects. We use the following form:

$$U_{XY}(R_{nm}) = 4\,\varepsilon^{XY}\left[\left(\frac{\sigma_{XY}}{R_{nm}}\right)^{12} - \left(\frac{\sigma_{XY}}{R_{nm}}\right)^{6}\right], \tag{10}$$

where $X$ and $Y$ stand for $A$ or $B$.

TABLE I. Lennard-Jones parameters $\varepsilon$ and $\sigma$ for a phase segregation (Ref. 13) for different values of $\Delta a/a$.

| | $\Delta a/a$ | $AA$ | $AB$ | $BB$ |
|---|---|---|---|---|
| $\varepsilon$ (meV) | | 180 | 153 | 146 |
| $\sigma$ (Å) | 0% | 2.3331 | 2.3331 | 2.3331 |
| $\sigma$ (Å) | 4% | 2.3331 | 2.3807 | 2.4283 |
| $\sigma$ (Å) | 6% | 2.3331 | 2.4052 | 2.4774 |
| $\sigma$ (Å) | 10% | 2.3331 | 2.4559 | 2.5787 |

The amplitude of elastic effects is controlled via the quantity $\Delta a/a$, corresponding to the lattice parameter difference between the pure $A$ and $B$ fcc phases. The following procedure is used to determine the potential parameters (for details see Ref. 13). We start with an alloy without atomic size mismatch: $\Delta a/a = 0\%$. In this case, $\sigma_{AA}$, $\sigma_{AB}$, and $\sigma_{BB}$ are equal and adjusted to reproduce a particular lattice parameter (0.361 5 nm here). The values of $\varepsilon^{\alpha\alpha}$ ($\alpha = A$ or $B$) are chosen to reproduce two given melting temperatures (1400 and 1155 K). Then, $\varepsilon^{AB}$ is fixed to ensure a phase separation at low temperature ($\varepsilon^{AA} + \varepsilon^{BB} - 2\varepsilon^{AB} \geqslant 0$). The value of $\Delta a/a$ is adjusted through $\sigma_{BB}$, with $\sigma_{AA}$ being kept constant. Then, $\sigma_{AB}$ is fixed to half the sum of $\sigma_{AA}$ and $\sigma_{BB}$. The other potential parameters are not modified. With such a procedure, the minimum value of each interaction potential remains unchanged when $\Delta a/a$ is varied. Detailed expressions of the second derivatives for a pair potential are given in Appendix A. The parameters obtained by this procedure, when interactions are limited to the fifth nearest neighbors, are given in Table I for different values of $\Delta a/a$.

We discuss now the behaviors of the chemical and elastic contributions of the EPIs for different size mismatches. First we emphasize that the interactions introduced above, referred to as chemical or elastic, are not intrinsic in nature. They depend on the reference state introduced above and around which a second-order expansion is performed. Therefore, when the size effect parameter $\Delta a/a$ is changed, both the elastic *and* chemical interactions change.

In Fig. 1, calculated values of EPIs are plotted as a function of the neighbor shell in real space for $\bar{c} = 0.10$ and $\frac{\Delta a}{a} = 0\%$, 4%, 6%, and 10%. Without atomic size mismatch, the elastic interactions vanish and the chemical interactions lead to a phase segregation. When $\frac{\Delta a}{a} \neq 0$, the elastic interactions become finite and their magnitude increases with the size mismatch. Besides, chemical interactions are seen to decay rapidly with distance, whereas elastic interactions decay very slowly. This long-range aspect of the EPIs due to the elastic interactions has been previously underlined in different studies at the atomic scale.[7,14–18]

In addition to the long-range behavior of the EPIs, elastic interactions may play a major role at short distances and therefore control the nature of the phase transition. When $\frac{\Delta a}{a} = 4\%$, the first neighbor elastic interaction contributes to

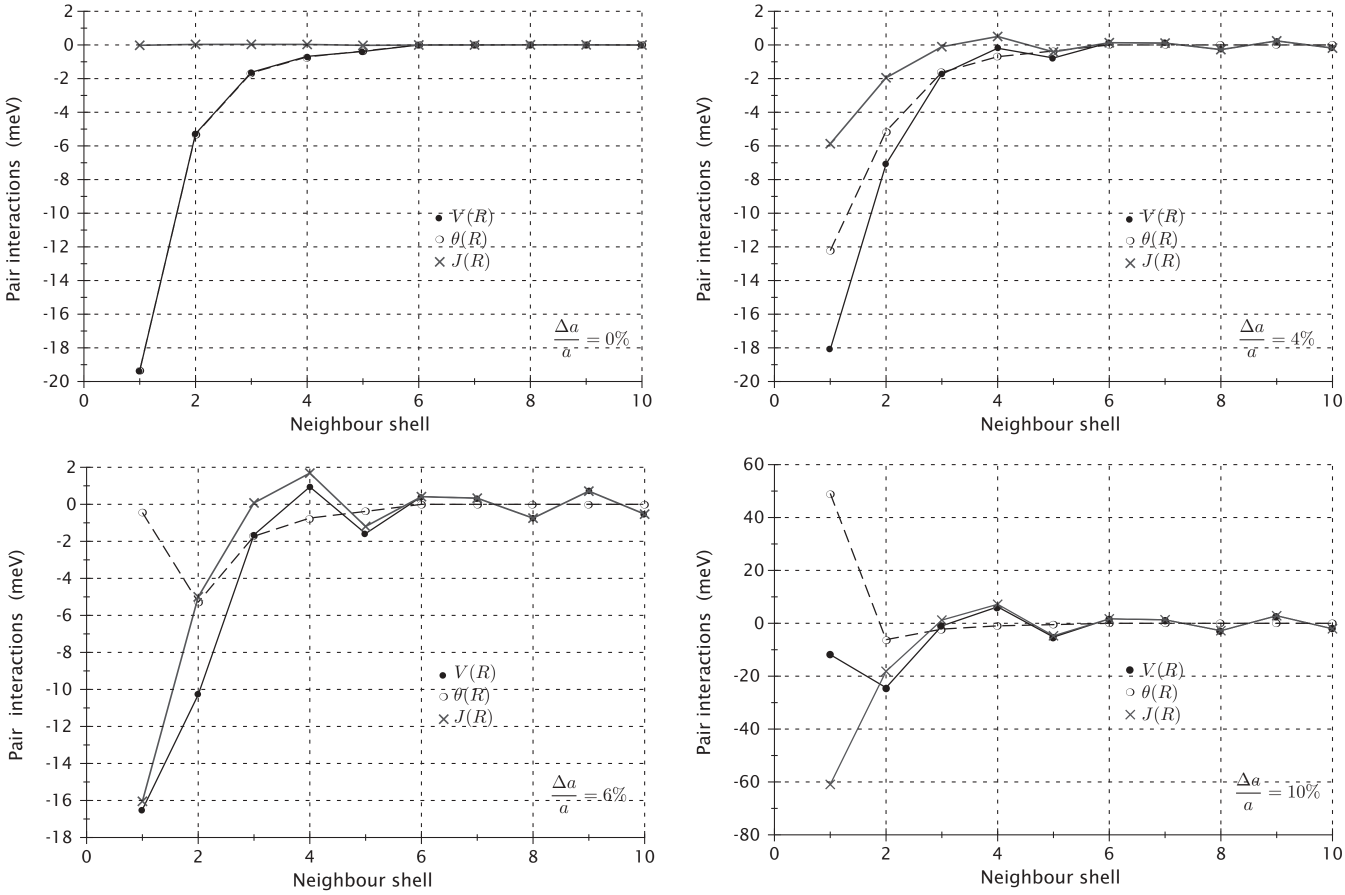

FIG. 1. Calculated values of the effective pair interactions $V(R)$, chemical interactions $\theta(R)$, and elastic interactions $J(R)$ for $\bar{c} = 0.10$ and $\frac{\Delta a}{a} = 0\%$, 4%, 6%, and 10%. The horizontal axis represents neighbor shells.

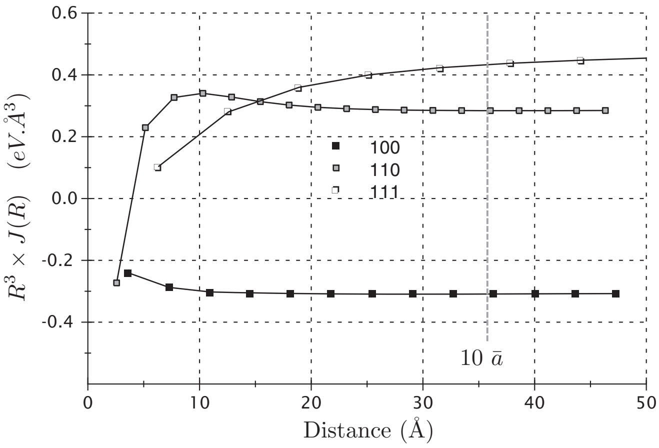

FIG. 2. Quantity $R^3 \times J(R)$ as a function of the atomic distance $R$ for three different crystallographic directions: (100), (110), and (111), for $\frac{\Delta a}{a} = 6\%$ and $\bar{c} = 0.10$.

one third of the total effective interactions. For $\frac{\Delta a}{a} = 6\%$, we note that the physical behavior of the system (phase separation again) is mostly controlled by the elastic contribution. This means that short-range elasticity can be essential for alloy thermodynamics, chemical and elastic contributions being eventually competitive (see, for example, $\frac{\Delta a}{a} = 10\%$ in Fig. 1). These features were also observed for EPIs calculated from EAM alloy energy[7] and with an second moment approximation - tight binding ising model (SMA-TBIM) approach[14] in the case of a Cu-Ag alloy. In brief, if the second-order expansion used above were limited to the chemical fluctuations $\delta c_n$, the induced effective Hamiltonian could lead to a thermodynamic equilibrium which is only approximatively reproduced, or even qualitatively wrong.

Finally, in order to characterize the crossover between the short-range and the long-range behaviors of elastic interactions, we display in Fig. 2 the quantity $R^3 \times J(R)$ as a function of the distance $R$ for $\frac{\Delta a}{a} = 6\%$. For large distances, the discrete interactions recover the $\frac{1}{R^3}$ decrease of the long-range elastic interactions, as expected within the continuum linear elasticity theory.[4,7] However, this regime is reached only for distances larger than about $10\bar{a}$. Therefore, the specific role of the long-range interactions on the microstructure evolutions (large spatial correlations and precipitate shapes) requires the use of a very large cutoff on the discrete real-space interactions. As discussed below, this necessitates an efficient numerical algorithm. Also, for smaller ranges, elastic interactions significantly deviate from their $1/R^3$ continuum linear elasticity behavior and, below $4\bar{a}$, the interaction anisotropy itself is qualitatively changed.

As a conclusion, we emphasize that a correct description of microstructure evolutions at small time and space scales requires an atomic scale approach, such as the one provided by the lattice statics formalism, when a size mismatch is present.

## III. MICROELASTICITY MODEL FROM MACROSCOPIC DATA

As explained above, when dealing with a specific alloy, the calibration of a realistic continuous interatomic potential can be necessary. Often this procedure is based on the fitting of relevant physical quantities (lattice parameters, elastic constants, cohesion energy, interface energy, etc.). This preliminary step is known to be particularly fastidious. Therefore it is highly desirable to develop a methodology to obtain elastic interactions directly from the macroscopic properties of the material of interest.

With this aim, we first recall[1,5,19] the link between the dynamical matrix and Kanzaki forces with elastic constants and an eigenstrain tensor. We then examine two different ways to obtain elastic interactions at the atomic scale. Finally, the two methods are compared numerically in the case of the model alloy already mentioned.

### A. Link between discrete and continuous approaches of elasticity

First of all, the connection of the Kanzaki forces and dynamical matrix with the macroscopic features of the material needs to be established. The case of the dynamical matrix is well known[19,20] and involves the elastic constants of the reference state:

$$\lambda^{R^0,\bar{c}}_{iklj} + \lambda^{R^0,\bar{c}}_{ilkj} = -\frac{1}{v_0}\sum_n \phi^{ij}_{0n}\, R^{0k}_n\, R^{0l}_n, \tag{11}$$

where translational invariance has been used and $v_0$ is the volume of the atomic cell. The notation $\{R^0,\bar{c}\}$ refers to a homogeneous state with an average lattice $R^0$, which is chosen in order to minimize $E_0(R,\bar{c})$ upon $R$. Using Eq. (11), the long-wavelength limit of the dynamical matrix is

$$\phi^{ij}(q \to 0) \simeq v_0\, \lambda^{R^0,\bar{c}}_{ikjl}\, q^k q^l = v_0 G^{-1}_{ij} \;\; \forall\, i,j, \tag{12}$$

where $G_{ij}(\mathbf{q})$ is, by definition, the continuous Green's function of the reference homogeneous state.

For Kanzaki forces, we start by expanding them up to the second order around $\mathbf{q} = 0$:

$$\psi^i(\mathbf{q}) = -i\, q^j \sum_n \psi^i_{0n}\, R^{0j}_n + o(q^2). \tag{13}$$

Kanzaki forces are the microscopic response to local concentration changes. Therefore, the identification of their link with macroscopic quantities requires the analysis of the stress or strain as a function of a given concentration change. A simple way is to compute the stress-free deformation of a homogeneous system when the average concentration is modified. We introduce an arbitrary inhomogeneous alloy $\{R',\bar{c}'\}$ with an average concentration $\bar{c}'$:

$$R'^i_n = R^{0i}_n + \bar{\epsilon}_{ij} R^{0j}_n + \delta u^i_n, \quad c'_n = c_n + \delta c_n. \tag{14}$$

By imposing $\delta u^i_n = 0$ at the boundaries or periodic boundary conditions on $\delta u^i_n$, $\bar{\epsilon}_{ij}$ refers to the macroscopic deformation and $\delta u^i_n$ are the local displacements. The energy of any alloy is then expanded up to the second order upon the reference state $\{R^0,\bar{c}\}$:

$$\begin{aligned} E = {} & E(R^0,\bar{c}) + E_{ch} \\ & + \sum_n \left.\frac{\partial^2 E}{\partial\bar{\epsilon}_{ij}\,\partial c_n}\right|_{\mathbf{R}^0,\bar{c}} \delta c_n \bar{\epsilon}_{ij} + \frac{1}{2}\left.\frac{\partial^2 E}{\partial\bar{\epsilon}_{ij}\partial\bar{\epsilon}_{kl}}\right|_{\mathbf{R}^0,\bar{c}} \bar{\epsilon}_{ij}\bar{\epsilon}_{kl} \\ & + \sum_{n,m} \psi^i_{nm}\delta c_n \delta u^i_m + \frac{1}{2}\sum_{n,m}\phi^{ij}_{nm}\delta u^i_n \delta u^j_m, \end{aligned} \tag{15}$$

where $E_{ch}$ is the chemical part.

First order and crossed terms vanish due to the symmetry properties of the lattice. Elastic relaxation is given by solving the sets of equations $\frac{\partial E}{\partial \bar{\epsilon}_{ik}} = 0$ (homogeneous relaxation) and $\frac{\partial E}{\partial \delta u_n^i} = 0$ (local relaxation). Let us consider the homogeneous relaxation only:

$$\begin{aligned}\frac{\partial E}{\partial \bar{\epsilon}_{ij}} &= \left.\frac{\partial^2 E}{\partial \bar{\epsilon}_{ij}\partial \bar{\epsilon}_{kl}}\right|_{R^0,\bar{c}} \bar{\epsilon}_{kl} + \sum_n \left.\frac{\partial^2 E}{\partial \bar{\epsilon}_{ij}\partial c_n}\right|_{R^0,\bar{c}} \delta c_n \\ &= N v_0 \lambda_{ijkl}^{R^0,\bar{c}}\, \bar{\epsilon}_{kl} + \sum_{n,m} \psi_{nm}^i R_m^{0j} \delta c_n \ = 0. \qquad (16)\end{aligned}$$

The components of the Kanzaki forces $\psi_{nm}^i$, defined in Eq. (3), do not depend on the alloy configuration, so they can be evaluated in a particular case. Let us assume that for all sites $n$, $\delta c_n = \overline{\delta c}$. To the lowest order, the average strain tensor $\bar{\epsilon}_{ij}$ is linked to $\overline{\delta c}$ by

$$\bar{\epsilon}_{ij} = \epsilon_{ij}^0 \overline{\delta c}, \qquad (17)$$

where $\epsilon_{ij}^0$ has the symmetry of the reference state. In the simple case of a phase separation and cubic symmetry $\epsilon_{ij}^0 = \epsilon^0\, \delta_{ij}$, where $\epsilon^0 = \frac{1}{\bar{a}(\bar{c})} \frac{d\bar{a}}{dc}|_{R^0,\bar{c}}$ is the Vegard coefficient. In the general case of an ordering system that displays different variants, $\epsilon_{ij}^0$ would be an appropriate average of the eigenstrain tensors associated with each variant. Finally, taking into account translational invariance, Eq. (16) becomes

$$\sum_m \psi_{0m}^i R_m^{0j} = -v_0\, \lambda_{ijkl}^{R^0,\bar{c}}\, \epsilon_{kl}^0. \qquad (18)$$

This equation establishes a general link between the macroscopic quantity $\epsilon_{kl}^0$ and the atomic scale Kanzaki forces.

### B. Elastic interactions from macroscopic data

In this section we examine two different ways to estimate microscopic elastic interactions directly from the value of macroscopic quantities.

The first method is simply based on the long-wavelength limit of the elastic interactions and has already been used to introduce elastic effects in the case of microscopic Mean-Field simulations.[21,22] Using Eq. (13), we obtain the following for $\mathbf{q} \to 0$:

$$J_{\mathrm{LS}}(\mathbf{q}) \sim -q^k \sum_n \psi_{0n}^i R_n^{0k}\, (\phi^{-1})^{ij}(\mathbf{q}) \sum_m \psi_{0m}^j R_m^{0l} q^l, \qquad (19)$$

where $J_{\mathrm{LS}}(\mathbf{q})$ refers to the elastic interactions obtained from an LS development. Here, the long-wavelength relations Eqs. (12) and (18) are inserted into Eq. (19) and, for $q \neq 0$, the discrete interactions can be formally written as

$$J_{\mathrm{LS}}(\mathbf{q}) \sim -v_0\, q^k \sigma_{ki}^0 G^{ij}(\mathbf{q}) \sigma_{jl}^0 q^l = v_0\, B(\mathbf{q}), \qquad (20)$$

where $\sigma_{ij}^0 = \lambda_{ijkl}^{R^0,\bar{c}}\ \epsilon_{kl}^0$. The quantities $B(\mathbf{q})$ are the usual Fourier transforms of elastic interactions that emerge within a homogeneous continuum elastic theory[1] when the average strain around the reference state is zero (see Sec. II A). The continuous interactions only depend on the direction of the $\mathbf{q}$ vector and their evaluation solely requires the knowledge of the elastic constants of the reference state and the eigenstrain $\epsilon_{ij}^0$ between the involved phases. Taking directly the continuous interactions $B(\mathbf{q})$ and using them through Eq. (20) at the atomic scale constitutes a first method to obtain elastic interactions from macroscopic data. We call this method the continuum limit approach (CLA) and note $J_{\mathrm{CLA}}(\mathbf{q}) = v_0\, B(\mathbf{q})$, the corresponding elastic interactions.

Even though the CLA provides correct elastic interactions at long range, it is bound to fail at short distances because is does not incorporate the discreteness of the lattice. Therefore we propose another scheme that still relies on Eqs. (11) and (18) but is based on a discrete atomic potential whose Kanzaki forces and dynamical matrix can be fitted on macroscopic elastic properties. As Kanzaki forces and the dynamical matrix are usually short ranged, we impose a cutting radius on these quantities. If this cutoff is short enough, the new quantities $\widetilde{\Psi}_{0n}^i$ and $\widetilde{\Phi}_{0n}^{ij}$ can be identified using only macroscopic parameters through Eqs. (11) and (18). In the following we detail the case of an isotropic pair potential, which is used for the numerical simulations.

With an isotropic pair potential, the quantities $\Psi_{nm}$ and $\Phi_{nm}$ adopt, for $R_n \neq 0$, the following forms:

$$\widetilde{\phi}_{0n}^{ij} = -\alpha\left(R_n^0\right) \delta_{ij} \ + \ \beta\left(R_n^0\right) \frac{R_n^{0i} R_n^{0j}}{R_n^{0^2}}, \qquad (21)$$

$$\widetilde{\psi}_{0n}^i = \delta\left(R_n^0\right) \frac{R_n^{0i}}{R_n^0}, \qquad (22)$$

where $R_n^0$ is the norm of the vector $\mathbf{R}_n^0$. The parameters $\alpha(R_n^0)$, $\beta(R_n^0)$, and $\gamma(R_n^0)$ are identified through Eqs. (11) and (18), and with the symmetry relation $\sum_n \widetilde{\phi}_{0n}^{ij} = 0$. More precisely, for each $N$-coordination shell, three parameters $\alpha_N$, $\beta_N$, and $\gamma_N$ have to be determined. The number of coordination shells to be considered needs to be large enough to reproduce all the elastic moduli of the material and the eigenstrain. The case of the fcc lattice is detailed in Appendix B. The quantities $\widetilde{\Psi}_{0n}^i$ and $\widetilde{\Phi}_{0n}^{ij}$ are then suitable to compute another set of elastic interactions, here called $J_{\mathrm{DLA}}(\mathbf{q})$. In the following, we refer to this method as the discrete lattice approach (DLA).

By construction, as they both rely on the long-wavelength limit $\mathbf{q} \to 0$, the CLA and DLA provide the same correct long-distance elastic interactions. However, contrary to the CLA, the DLA, which incorporates the discrete nature of the lattice, is expected to give a more reliable description at short distances, as confirmed below.

### C. Comparison of elastic interactions

In this section, a numerical comparison of the LS interactions $J_{\mathrm{LS}}$ with the CLA interactions $J_{\mathrm{CLA}}$ and the DLA interactions $J_{\mathrm{DLA}}$ is proposed, using a Lennard-Jones pair potential. The potential parameters used are listed in Table II.

TABLE II. Lennard-Jones potential parameters $\varepsilon$ and $\sigma$ used for elastic interaction calculation. The atomic size effect is 6%, and $a$ designates the lattice parameter of the fcc structure.

| | $AA$ | $AB$ | $BB$ |
|---|---|---|---|
| $\varepsilon$ (meV) | 180 | 153 | 146 |
| $\sigma$ (Å) | 2.3331 | 2.4052 | 2.4774 |
| $a$ (Å) | 3.6153 | | 3.8390 |

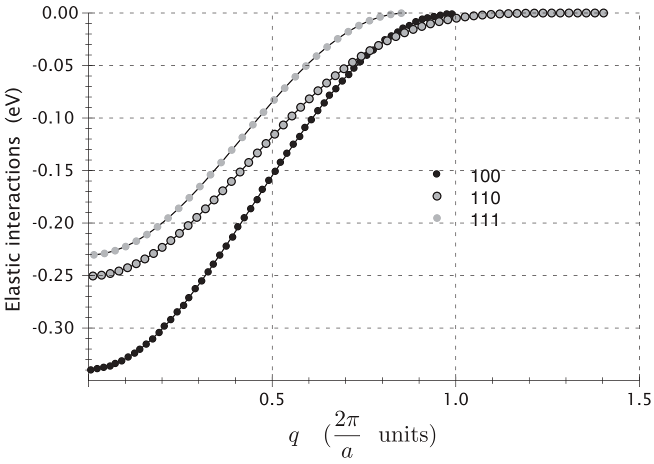

FIG. 3. Fourier transforms of elastic interactions $J_{\mathrm{LS}}(\mathbf{q})$ for $\frac{\Delta a}{a} = 6\%$ and $\bar{c} = 0.06$ along (100), (110), and (111) directions of the reciprocal space. $J_{\mathrm{LS}}(\mathbf{q})$ is defined in the first Brillouin zone. The three curves end at the special points.

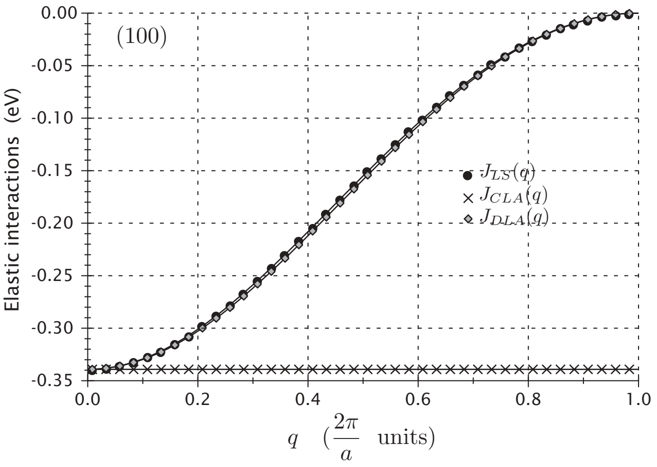

FIG. 4. Elastic interactions for $\frac{\Delta a}{a} = 6\%$ and $\bar{c} = 0.06$, calculated by different methods: lattice statics analysis $J_{\mathrm{LS}}$ (black circles), discrete lattice approximation $J_{\mathrm{DLA}}$ (gray squares), and continuous limit approximation $J_{\mathrm{CLA}}$ (black crosses). They are represented in the (100) direction of the reciprocal space.

In the real space, the range of the Lennard-Jones potential is limited to the fifth neighbors. The atomic size effect between the pure components is fixed at 6%. The elastic constants for the reference state at concentration $\bar{c} = 0.06$ are $C_{11} = 215$ GPa, $C_{12} = C_{44} = 122$ GPa. The lattice parameter is $\bar{a} = 3.630\,2$ Å, and the eigenstrain tensor at this concentration is $\epsilon^0_{ij} = 0.068\,0\,\delta_{ij}$. A common approximation that can be found in the literature[22,23] is to assume that the lattice parameter varies linearly with concentration over the whole composition range. In our case this linear behavior is rather well followed and leads to an error on the equilibrium lattice parameter lower than 0.05% at $\bar{c} = 0.06$. However the value of the eigenstrain $\epsilon^0_{ij}(\bar{c})$ is much more sensitive to the precise shape of the $\bar{a}(\bar{c})$ curve. Assuming a strictly linear behavior of the lattice parameter leads to a relative error of 9.5%. Such an error would induce a more than 18% error on the long-wavelength limit of the elastic interactions.

We first examine the calculated values of the $J_{\mathrm{LS}}(\mathbf{q})$, represented in Fig. 3, along specific directions of the reciprocal space. We first note that $J_{\mathrm{LS}}(\mathbf{q})$ is equal to zero at special points, as expected (see Ref. 7). When looking at the overall behavior of $J_{\mathrm{LS}}(\mathbf{q})$, we see that its value depends both on the norm and the direction of the $\mathbf{q}$ vector. The directional dependence is reminiscent of anisotropic elasticity. The dependence with respect to the norm indicates that the short-range elastic interactions do not scale with the long-range ones. The latter are embedded in the norm-independent long-wavelength limit $\mathbf{q} \to 0$ of $J_{\mathrm{LS}}(\mathbf{q})$.

We now compare the CLA and the DLA with the LS method. Figure 4 shows the elastic interactions for all the methods in the (100) direction of the reciprocal space. For the DLA, we have limited the real-space range of the Kanzaki forces and dynamical matrix to the next-nearest neighbors (see Appendix B for details). As expected, in the long-wavelength limit $q \to 0$, all the interactions converge to the same value. However, the long-wavelength regime is limited to a small $\mathbf{q}$ domain, as already mentioned in Sec. II B. For $q \neq 0$, CLA interactions strongly differ from the exact LS ones. So, as anticipated above, the relevance of this method for the short-range elastic interactions is poor. On the other hand, the DLA interactions follow the LS ones with a very good agreement for the entire range of $\mathbf{q}$. These observations are still valid for the other directions (110) and (111).

In Fig. 5 we present, as a function of distance, the real-space EPIs calculated within the previous approaches. These EPIs include both elastic and chemical contributions, the latter being of course the same in the three cases. We observe that the DLA provides a very good approximation of the exact LS, whereas the CLA shows an important deviation (33%) for the first neighbor interactions, which are the dominant ones. As a consequence, the phase diagram corresponding to the CLA interactions would strongly differ from the LS phase diagram. This would impact both the volume fraction of precipitates and the kinetics of evolving microstructures.

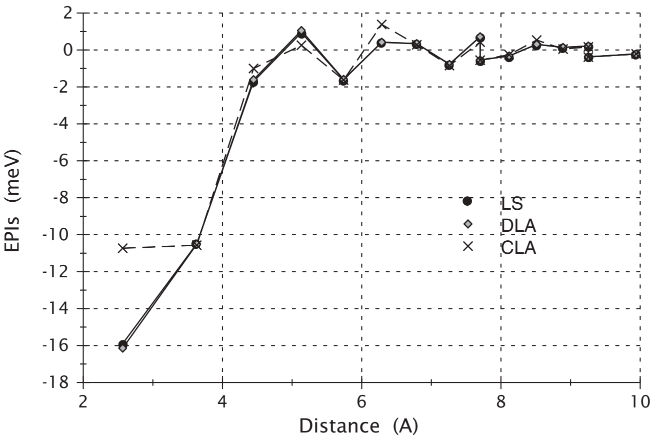

FIG. 5. Effective pair interactions plotted versus the atomic distance in angstroms for $\frac{\Delta a}{a} = 6\%$ and $\bar{c} = 0.06$, calculated by different methods: LS (black circles), DLA (gray squares), and CLA (black crosses).

```
$i = 1, n_{main}$
    Re-initialization of $\Delta E_{pq}$
    according to Eq. (23)
    $n = 1, n_{ising}$
        Exchange between first neighbors
        If acceptance: updating procedure
        according to Eq. (25)
```

FIG. 6. Scheme of the quadrupolar algorithm convenient for long-range interactions. We have $n_{\rm Ising} = K \times N_{\rm sites}$ with $K \sim 10^3$ and $n_{\rm main} = {\rm MCS}/K$.

### D. Discussion

The main advantage of the lattice statics approach is to embed the elastic forces into effective interactions that couple discrete degrees of freedom. The lattice statics approach, which is an atomic scale linear elasticity theory, should converge to the continuum elastic theory in the long-wavelength limit. This point has been numerically confirmed in our analysis. However, for a specific alloy, the numerical implementation of the method requires the knowledge of a detailed potential at the atomic scale, which is often very difficult to obtain.

As shown above, the DLA provides an efficient way to circumvent this difficulty, as the calculation of the corresponding discrete elastic interactions simply requires knowledge of a few macroscopic quantities extracted from experiments or *ab initio* calculations. The procedure relies on the identification of short-range Kanzaki forces and the dynamical matrix. In the present paper, this has been done within a pair potential framework. This restricts the analysis to systems which approximately follow the Cauchy rule. More general situations, that do not suppose a specific form for an underlying potential, can be straightforwardly considered. This point is addressed in Sec. IV D.

## IV. MICROSTRUCTURE SIMULATIONS

Our purpose is now to simulate, at the atomic scale, the microstructure evolution in the presence of atomic size mismatch.

### A. Computational details

We use a Monte Carlo scheme in which energies are computed with the EPIs previously determined. For the sake of simplicity, we choose a Kawasaki dynamics. Simulations are performed in the canonical ensemble. For each attempt of atom exchange, we need to evaluate the energy cost $\Delta E_{p_0 q_0}$

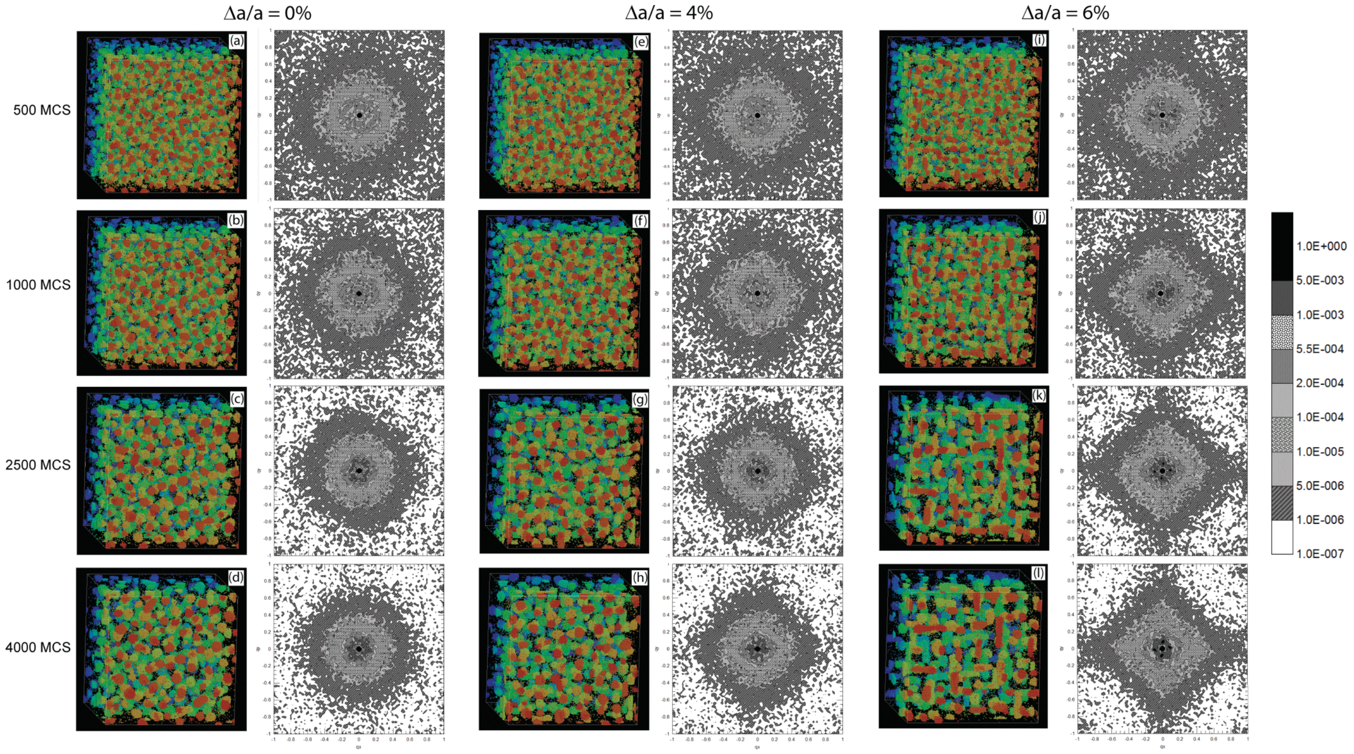

FIG. 7. (Color online) Snapshots of microstructures extracted at four Monte Carlo times (MCS) from simulations at 300 K for binary alloys with a nominal concentration $\bar{c} = 0.08$ and with different atomic size mismatches: (a)–(d) corresponds to $\frac{\Delta a}{a} = 0\%$, (e)–(h) to $\frac{\Delta a}{a} = 4\%$, and (i)–(l) to $\frac{\Delta a}{a} = 6\%$. For the sake of clarity, only one type of atom is represented and the color is a function of the depth in the simulation box, whose size is (29 nm).[3] The Fourier transform in the (001) plane is represented for each microstructure (see text for details). Each component of the $\mathbf{q}$ vector extends from $-2\pi/\bar{a}$ to $2\pi/\bar{a}$, and the scale for intensity is shown on the right side bar.

given by

$$\Delta E_{p_0q_0} = (\delta c_{q_0} - \delta c_{p_0})[H_{p_0,q_0} + V_{q_0p_0}(\delta c_{p_0} - \delta c_{q_0})]$$

$$\text{with} \quad H_{p_0,q_0} = \sum_n \{V_{p_0n} - V_{q_0n}\}\delta c_n, \tag{23}$$

where $\{p_0,q_0\}$ is the pair of nearest neighbors we try to exchange.

The numerical implementation requires the choice of a cutoff. As recalled above, the long-wavelength elastic interactions $V_{nm}$ decrease as $1/R^3$. However, within an exchange dynamics, the energy cost $\Delta E_{p_0q_0}$ consists in summing individual components $(V_{p_0n} - V_{q_0n})$ which decrease as $1/R^4$. Therefore, the sum in Eq. (23) converges *absolutely* and consequently can be approximated by the choice of a finite cutoff. In the present case, we found that $r_{\text{cut}} = 15\bar{a}$ was a large enough value to correctly reproduce spatial correlations between precipitates (the observed microstructures were hardly sensitive to $r_{\text{cut}}$ in the range 11–20$\bar{a}$). However, with such a cutoff, the sum over $n$ in Eq. (23) includes approximatively 20 000 terms. Different algorithms are available in the literature to reduce the CPU time devoted to this summation.[16,24] We have implemented the Fratzl and Penrose[16] algorithm, well suited for the Kawasaki dynamics. The initial step is to compute and store the energy costs $\Delta E_{pq}$ for all the first-nearest-neighbor pairs. Then the algorithm proceeds as follows: Once an exchange $\{p_0,q_0\}$ has been accepted, the array $\Delta E_{pq}$ is updated according to

$$\Delta E_{pq} = (\delta c_q - \delta c_p)\widetilde{H}_{p,q} - (\delta c_q - \delta c_p)V_{qp}, \tag{24}$$

with

$$\widetilde{H}_{p,q} = H_{p,q} + (\delta c_{q_0} - \delta c_{p_0})[V_{p_0p} - V_{q_0p} + V_{q_0q} - V_{p_0q}]. \tag{25}$$

We observe that the variation of the energy cost $\Delta E_{pq}$ induced by the $\{p_0,q_0\}$ exchange is concentrated in a quadrupolarlike term that decreases as $1/R^5$ if the pairs $\{p,q\}$ and $\{p_0,q_0\}$ are far enough from each other. Therefore, we may limit the updating procedure of the array $\Delta E_{pq}$ within a sphere centered on $\{p_0,q_0\}$ with a smaller radius (here 8$\bar{a}$) than the cutoff used in the initialization of the array $\Delta E_{pq}$. This greatly improves the CPU efficiency of the overall algorithm. However, in order to avoid a systematic drift for very long runs, we found it necessary to reinitialize periodically the array $\Delta E_{pq}$ using Eq. (23) [typically every 1000 Monte Carlo steps[25] (MCS)]. The implementation of this scheme in the Monte Carlo code is summarized in Fig. 6.

As this algorithm is based on the storage of the energy costs of all first neighbor pair exchanges, its efficiency increases when the number of accepted exchanges decreases, i.e., at low temperature. Finally, we mention that the extension of this algorithm to multicomponent alloys is straightforward.

Afterward, the overall microstructure morphologies are represented by monitoring configurations at different times along the precipitation sequences. Kinetic aspects are quantitatively analyzed using the number of precipitates as a function of the simulation time. Precipitates are defined through the computation of a local concentration field. The local average concentration $\bar{c}_n$ at site $n$ is defined as the arithmetic average of the occupancies over its first and second neighbors. Site $n$ is supposed to sit within a precipitate if $c_n \geqslant 0.5$. Also, the anisotropy of the microstructure (precipitate shapes and spatial correlations) may be qualitatively identified by computing the diffuse intensity along particular directions in the Fourier space:

$$I(\mathbf{q}) = \sum_n \left| f_n \, e^{i\mathbf{q}\cdot\mathbf{R}_n^0} \right|^2, \tag{26}$$

where $\mathbf{q}$ is a vector within the first Brillouin zone. $f_n$ is an effective diffusion length of the atom that sits at $R_n^0$ (here, $f_n = 1$ if site $n$ is inside a precipitate, 0 otherwise). Such an analysis in Fourier space has many features in common with small angle scattering experiments.[26] Indeed, the intensity diffused at large $q$ values is associated with the shape of the precipitates, whereas the intensity at intermediate $q$ values also includes information on the spatial correlations between precipitates. Nevertheless, such an analysis is possible only when the corresponding characteristic lengths (precipitate sizes and correlation lengths) are sufficiently distinct.

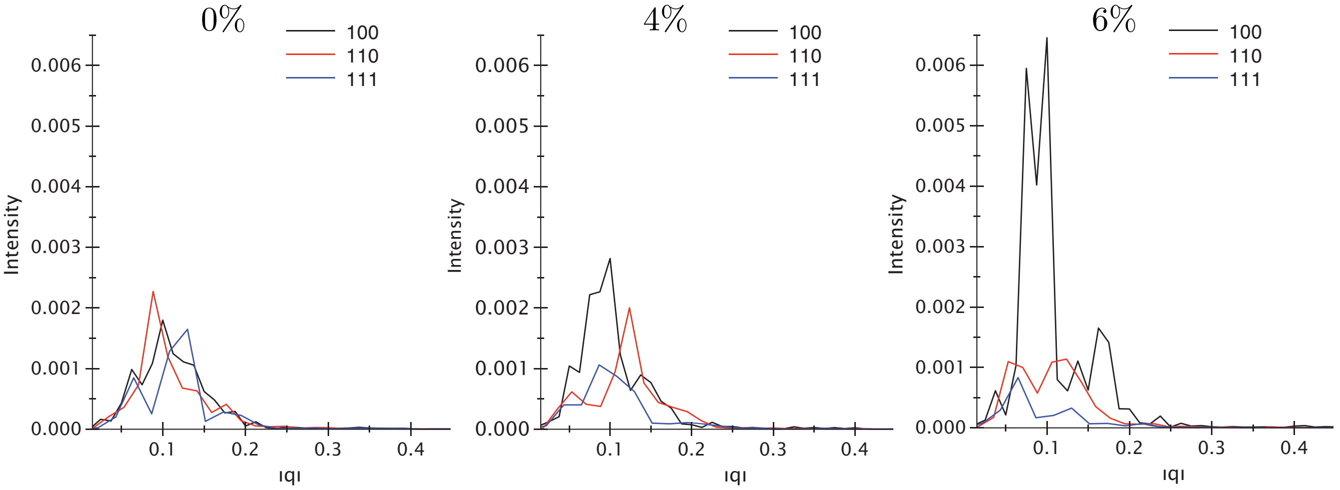

FIG. 8. (Color online) Fourier analysis of microstructures obtained for $\frac{\Delta a}{a} = 0\%$, 4%, and 6%, after 4000 MCS. Diffused intensity is plotted versus the norm of the $\mathbf{q}$ vector, in $\frac{2\pi}{a}$ units along the (100), (110), and (111) directions.

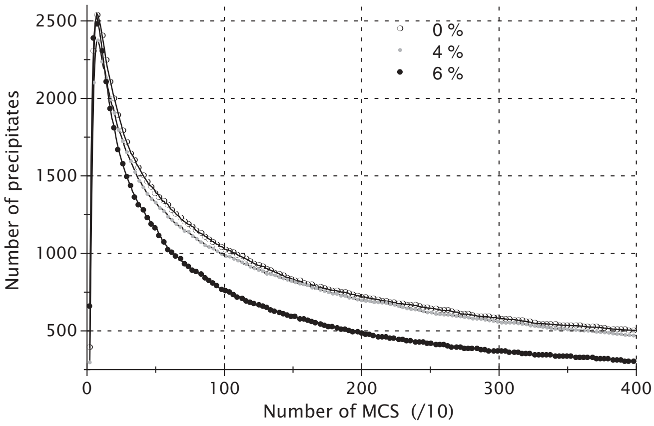

FIG. 9. Time evolution of the number of precipitates for binary alloys with $\frac{\Delta a}{a} = 0\%$, 4%, and 6% and with $\bar{c} = 0.08$.

### B. Influence of atomic size effect on microstructure

The set of EPIs calculated with the potential parameters listed in Table I is now used to investigate the role of the atomic size mismatch on microstructure morphology. We perform our simulations on fcc boxes whose size is $80\bar{a} \times 80\bar{a} \times 80\bar{a}$ (i.e., 2 048 000 atoms), where $\bar{a}$ is the lattice parameter of the reference state. In this section, we consider three binary alloys at 300 K with an average concentration $\bar{c} = 0.08$. For the first alloy, the atomic size mismatch $\frac{\Delta a}{a}$ is zero, whereas it is 4% and 6% for the others. The corresponding values of $\bar{a}$ are 3.615 Å, 3.627 Å, and 3.635 Å, respectively. The initial configuration of the simulations is a random solid solution. Figure 7 shows, for each alloy, the configurations extracted from the Monte Carlo simulations at 500, 1000, 2500, and 4000 MCS and the corresponding maps in the Fourier space in the [001] zone axis. Without atomic size mismatch [Figs. 7(a)–7(d)], precipitates are spheric and randomly distributed in the simulation box. This is confirmed by the circular symmetry of the diffraction pattern, both in the domain of large $q$, which is sensitive to the shape of precipitates, and at intermediate $q$, i.e., in the domain which is sensitive to spatial correlations between precipitates [see Fig. 8(a)]. This also implies that the interface free energy is isotropic at this temperature. For $\frac{\Delta a}{a} = 4\%$ and $t = 500$ MCS, the microstructure in real space appears to be very similar to the one obtained in the absence of atomic size mismatch. However, the slight anisotropy at large $q$ in the diffraction pattern reveals that precipitates are in fact slightly cuboidal. At later times, we observe larger precipitates which are aligned along cubic directions, as confirmed by the anisotropy of the diffracted intensity profiles shown in Fig. 8(b). When $\Delta a/a = 6\%$, and at early time (500 MCS), precipitates definitely adopt anisotropic shapes and alignments along cubic directions are already clearly visible. At later times, anisotropy of the precipitate shape develops and they often show elongated shapes along cubic directions. Their cross section is almost square and interfaces are oriented along $\{100\}$ planes. At further times (not shown here), we have observed that the shape of the precipitates evolves toward a platelike shape. In this case, the diffraction pattern exhibits a cross shape with axes oriented along the $\langle 100 \rangle$ directions. Precipitate shapes and alignments are the result of elastic relaxations which are driven by the elastically soft directions, here $\langle 100 \rangle$ because of a negative elastic anisotropy ($C_{11}$-$C_{12}$-$2C_{44}$).

The number of precipitates versus simulation time, extracted from the simulations described above, is given in Fig. 9. For all investigated atomic size mismatches, the number of precipitates features a peak at early times followed by a monotonous decrease. This behavior is characteristic of a nucleation-growth process. Note also that the number of precipitates in the simulations at long times decreases when the atomic size mismatch increases. This point is consistent with the anisotropic coalescence/coagulation of precipitates induced by elastic relaxations. A more quantitative analysis is however difficult to perform, as the solubility limits for the three alloys slightly differ (0.007, 0.007 5, and 0.008 for the alloys with $\Delta a/a = 0\%$, 4%, and 6%, respectively). Finally, the analysis of the time evolution of precipitate sizes (not shown here) reveals that the asymptotic regime[27,28] is not reached at the end of our simulations ($t = 4000$ MCS).

In brief, we have shown that our implementation of the lattice statics technique using the Fratlz *et al.* algorithm

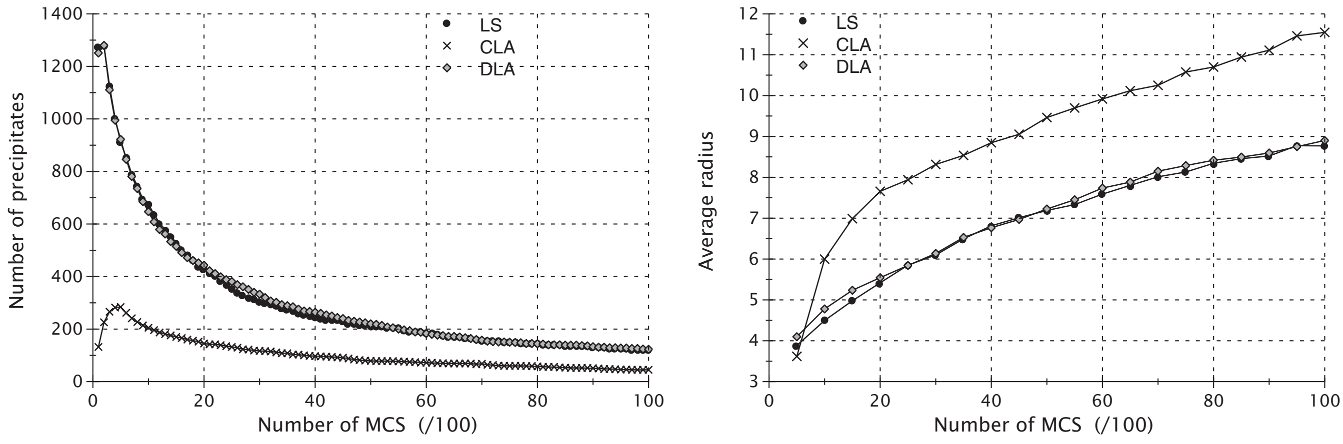

FIG. 10. Number of precipitates (left) and average radius (right) in angstroms versus Monte Carlo time for alloys with $\frac{\Delta a}{a} = 6\%$ and $\bar{c} = 0.06$ using the LS, CLA, and DLA interactions.

allows study of the microstructural evolutions of coherent alloys with elastic effects using thermodynamics simulations at the atomic scale. In particular, we have shown that the morphological modifications of the precipitate shapes and the development of spatial correlations between precipitates are correctly accounted for. This technique is well adapted to investigate the first stages of the precipitation process (incubation, nucleation), these regimes being difficult to explore with modeling based on continuous approaches.

### C. Microstructures obtained with different methods for elastic interaction calculations

In this section, we compare the microstructural evolutions obtained with the LS, CLA, and DLA interactions. As detailed in Sec. III C, the LS method is an exact derivation of coherent elasticity at the atomic scale from a continuous potential, the CLA is derived from the continuum limit of elastic interactions, and the DLA verifies the long-wavelength relations [Eqs. (11) and (18)] but also includes the discreteness of the lattice. These approaches are applied to the same

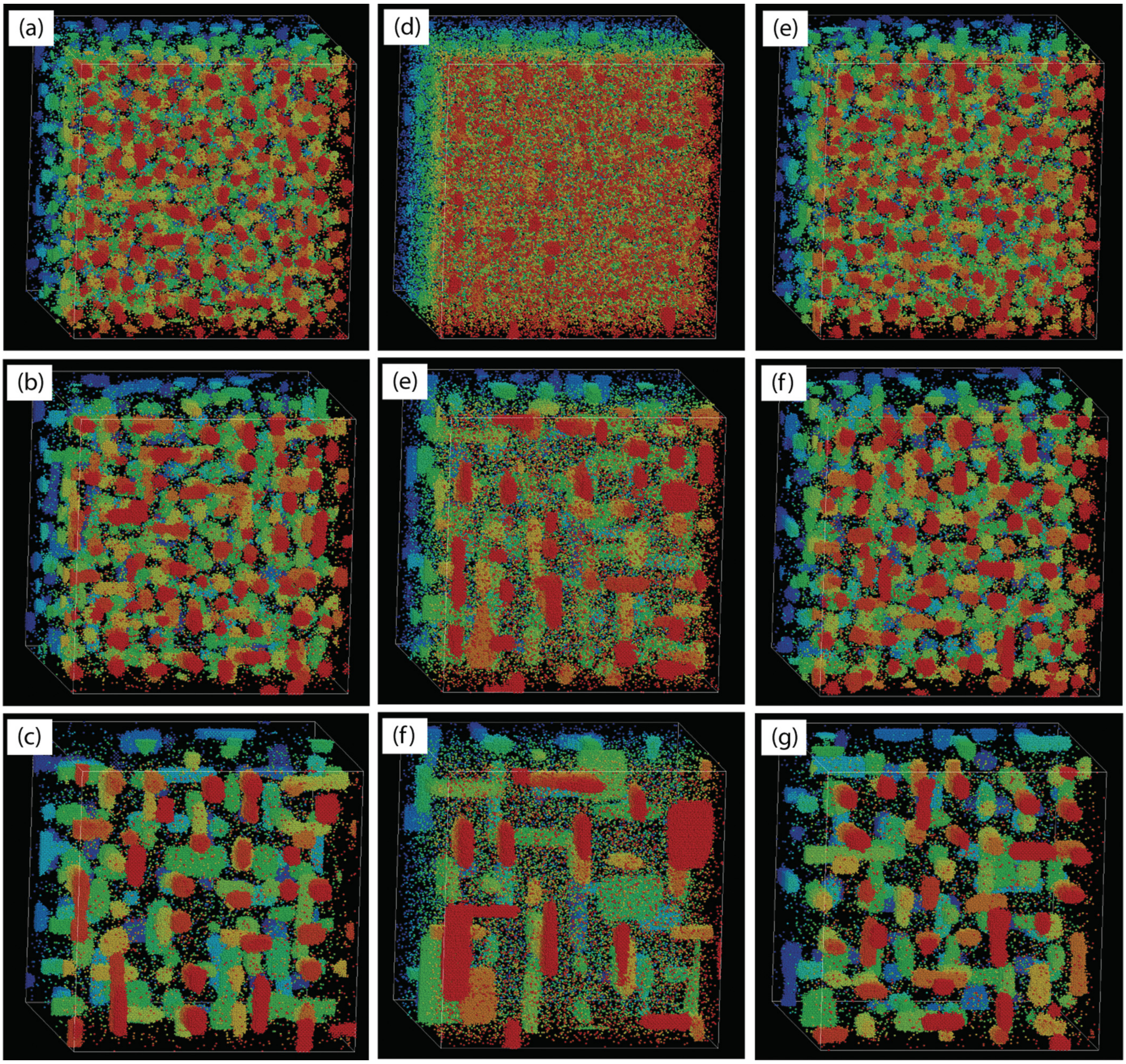

FIG. 11. (Color online) Snapshots of microstructures extracted at 500, 2000, and 10 000 MCS from Monte Carlo simulations at 300 K for binary alloys with a nominal concentration $\bar{c} = 0.06$ and with an atomic size mismatch $\frac{\Delta a}{a} = 6\%$. Images (a)–(c) correspond to the calculations with the exact lattice statics (LS) interactions. Images (d)–(f) and (g)–(i) correspond to the calculations with the CLA and the DLA approximations, respectively (see text for details). For the sake of clarity, only one type of atom is represented and the color is a function of the depth in the simulation box, whose size is (29 nm)$^3$.

alloy with an atomic size mismatch of 6% and a nominal composition $\bar{c} = 0.06$. The values of the elastic and total interactions are those discussed in Sec. III C and displayed in Figs. 4 and 5. We also recall that the chemical part of the EPIs is the same in the three cases.

As shown in Fig. 5, the CLA value of the EPI for the first neighboring distance strongly differs from the LS and DLA interactions. As a consequence, the solubility limits in the CLA are expected to be different from those corresponding to the other methods. This is confirmed by the values of the matrix composition measured in the later stages of our simulations (0.031 for the CLA, 0.008 otherwise). This difference necessarily impacts the precipitation driving forces. The analysis of Fig. 10, that displays the time evolution of the number of precipitates and their average radius at 300 K, confirms that the kinetics of precipitation is correctly reproduced by the DLA whereas the CLA leads to a quantitative error. Indeed, within the CLA, precipitates are fewer and larger during the whole time range investigated.

Figure 11 represents the snapshots of the configurations extracted from the Monte Carlo simulations at $t = 500$, 2000, and 10 000 MCS for the three methods. The microstructural evolutions calculated with the LS and the DLA interactions are very close and no significant differences can be observed. Precipitates, initially almost spheric when they are small ($t =$ 500 MCS), adopt elongated shapes along one cubic direction when they grow. For the CLA, strongly anisotropic precipitates are already seen for $t = 2000$ MCS. In addition, they evolve towards platelets around $t = 10\,000$ MCS (elongation along two cubic directions). These shapes minimize the elastic energy of isolated precipitates within homogeneous elasticity theory.[1] Such differences are more quantitatively evidenced by the analysis of the individual morphologies of the inclusions. Since the precipitates are well separated, this can be done through the calculation of their shape factors defined as follows. First, the characteristic length of the precipitate in each cubic direction is computed as the standard deviation of the corresponding coordinate. Then, using the three obtained sizes $l_1 \leqslant l_2 \leqslant l_3$, the shape factors $F_1$ and $F_2$ are defined by

$$F_1 = \frac{l_3}{l_1} \qquad \text{and} \qquad F_2 = \frac{l_2}{l_1}. \tag{27}$$

The quantities $F_1$ and $F_2$ allow differentiation between cubic or spheric precipitates ($F_1 \simeq F_2 \simeq 1$) from precipitates elongated in one or two cubic directions ($F_1 \geqslant F_2 \simeq 1$ and $F_1 \simeq F_2 \geqslant 1$, respectively). A each time step, the average shape factors $< F_1 >$ and $< F_2 >$ of the precipitates in the simulation box are computed. Their time evolution is represented in Fig. 12. Again, the behaviors corresponding to the LS and the DLA interactions are very similar on the whole time scale investigated. Precipitates evolve from an almost isotropic shape ($< F_1 > \approx < F_2 > \approx 1.2$ at $t = 500$ MCS) to an anisotropic one-dimensional shape ($< F_1 > \approx 2$, $< F_2 > \approx 1.2$ at $t = 6000$ MCS). With the CLA interactions, the shape factors, initially close to those observed for the LS and the DLA interactions, display a much sharper increase with time. This is mostly a consequence of the too-high solubility limit predicted by the CLA. As mentioned above, this leads to the precipitation of larger precipitates which adopt platelike shapes to minimize the coherent elastic energy.

In brief, we have shown that the simple extension of continuum linear elasticity down to the atomic scale (CLA) fails to reproduce the correct precipitation processes. The method proposed here (DLA) provides a very good approximation of the exact LS analysis, even when elastic effects are strong ($\Delta a/a = 6\%$ here).

### D. Generalization of the DLA

In this paper, the identification of short-range Kanzaki forces and dynamical matrix from macroscopic quantities, as required by the DLA, has been performed within a pair potential framework. This limits the range of application of such a method to a few materials. A more general derivation for $\widetilde{\psi}$ and $\widetilde{\phi}$ can be done by considering the form they adopt for the first neighbors in an fcc lattice. We give their expression for the [110] first neighbor pair, the others being straightforwardly obtained using symmetry relations between the 12 pairs that belong to the first neighbor shell:

$$\widetilde{\phi}^{ij}_{0,[110]} = \begin{pmatrix} \alpha & \gamma & 0 \\ \gamma & \alpha & 0 \\ 0 & 0 & \beta \end{pmatrix}, \tag{28}$$

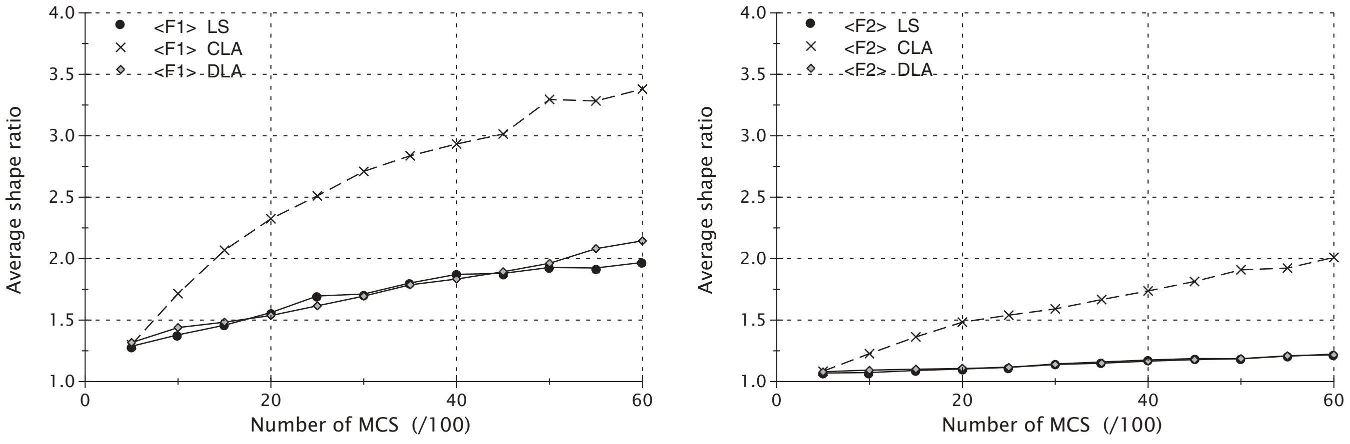

FIG. 12. Average shape ratios $< F_1 >$ (left) and $< F_2 >$ (right) versus MCS for alloys with $\frac{\Delta a}{a} = 6\%$ and $\bar{c} = 0.06$ using the LS, CLA, and DLA interactions.

$$\widetilde{\psi}^{i}_{0,[110]} = \begin{pmatrix} \delta \\ \delta \\ 0 \end{pmatrix}. \tag{29}$$

The number of non-null and independent coefficients in Eqs. (28) and (29) is a consequence of the fcc lattice symmetries and symmetry rules $\widetilde{\phi}^{ij}_{0n} = \widetilde{\phi}^{ji}_{0n} = \widetilde{\phi}^{ij}_{n0}$. The insertion of $\widetilde{\psi}$ and $\widetilde{\phi}$ into Eqs. (11) and (18), limited to the first neighbor shell in the fcc lattice, leads to a set of linearly independent equations that links the unknown atomic scale quantities $\alpha$, $\beta$, $\gamma$, and $\delta$ to the macroscopic elastic coefficients $C_{11}$, $C_{12}$, $C_{44}$ and to the eigenstrain tensor $\epsilon^0_{ij}$:

$$\begin{aligned} \alpha &= -\frac{\bar{a}}{4}C_{11}, \quad \beta = \frac{\bar{a}}{4}(C_{11} - 2C_{44}), \\ \gamma &= -\frac{\bar{a}}{4}(C_{12} + C_{44}), \quad \delta = -\frac{\bar{a}^2}{16}\epsilon^0(C_{11} + 2C_{12}). \end{aligned} \tag{30}$$

To summarize, the proposed general DLA consists simply in identifying, through Eqs. (28) and (29), the first neighbor Kanzaki forces and dynamical matrix, which when inserted through their Fourier transform into Eq. (9), allow the discrete elastic interactions $J_{\mathrm{DLA}}(\mathbf{q})$ to be obtained. Therefore, the DLA provides a general and straightforward scheme to identify atomic scale elastic interactions that not only reproduce the long-range elastic behavior, but also incorporate the correct short-range elastic interactions that are bound to the discrete nature of the lattice. This is a prerequisite to correctly simulate precipitation processes, from the early stages to the latter ones. This methodology is easily transferable to other type of lattices than the fcc one, and thus to other type of materials.

## V. CONCLUSION

Long-range elasticity is a major driving force during microstructural evolution of alloys when atomic size mismatch is present. Elastic effects can also be in competition with chemical effects at short-range distances, contributing to the stability of the alloy.

The lattice statics approach provides a simple energetic model to compute alloy properties using statistical methods (here, Monte Carlo simulations). Starting from a continuous potential description of alloy energetics and using lattice Green's functions, effective pair interactions depending only on compositional degrees of freedom are derived. In this study we use a numerical algorithm which allows one to calculate microstructural evolutions on large time and space scales. Using different atomic size mismatches, we show that the major trends associated with elasticity (precipitate shapes and spatial correlations) are correctly reproduced from the nucleation and growth regime to the beginning of coarsening.

Also, to avoid the long development of a specific continuous potential, we propose a general method, here called the discrete lattice approach (DLA), to calibrate atomic scale elastic interactions using only a few macroscopic properties of the alloy (elastic moduli, eigenstrain tensor). Contrary to the method which consists in using, down to the atomic scale, the elastic interactions derived from linear elasticity (here referred to as the CLA), the DLA provides an accurate description of short-range elasticity. We show in this paper that the DLA gives a very good approximation of the exact lattice statics method. This point is quantitatively verified on both the EPIs values and the microstructural evolutions. To complete the calibration of the energetic model, chemical pair interactions can be obtained from *ab initio* calculations (cluster expansion[29,30]) or diffuse x-ray scattering experiments.[31]

Many interesting prospects follow our work. First of all, the implementation of a realistic kinetic mechanism, involving exchanges between atoms and vacancies, is needed to correctly reproduce physical phenomena like solute drag, migration of small clusters, or vacancy surface trapping. This could be done by identifying a vacancy to an additional alloying element. Within such a framework, realistic kinetic Monte Carlo simulations taking into account elasticity could be performed for alloys with atomic size mismatch, allowing relevant comparisons with three-dimensional atom probe experiments.

Another interesting perspective is the extension of the LS formalism to topological defects, such as dislocations, within the framework of the DLA. In this study, alloys have always been considered as coherent materials. When coherency stress becomes too high, dislocations can relax the stored elastic energy when the plastic threshold is reached. As pointed out by Nabarro,[32] a dislocation loop produces the same displacement field as a platelet inclusion, with a stress-free eigenstrain related to the Burgers vector $\mathbf{b}$ and the normal $\mathbf{n}$ of the loop by $\epsilon^{00}_{ij} = \frac{1}{2}\frac{b_i n_j + b_j n_i}{d}$, where $d$ is the interplanar distance along direction $\mathbf{n}$. This approach has been applied at the mesoscopic scale with phase field methods (see, for example, Refs. 33 and 34). This formalism, transposed down to the atomic scale within the DLA, gives an interesting way to study coherency loss phenomena or the interplay between an evolving elastic microstructure and plastic relaxation through dislocation glide. The significant advantage of the present discrete approach, as opposed to a phase field one, is that small-scale phenomena (such as dislocation nucleation and annihilation, interactions between dislocations and point defects, or thin interfaces) are readily taken into account. A nonconserved spin-flip dynamic, corresponding to the presence or absence of the dislocation loop, could make this formalism compatible with a lattice Monte Carlo scheme.

## APPENDIX A: SECOND DERIVATIVES

In this appendix, the different second derivatives of the energy with respect to atomic displacements and chemical degrees of freedom are detailed in the case of a pair potential. Chemical interactions:

$$\theta_{nm} = U_{AA}(R^0_{nm}) + U_{BB}(R^0_{nm}) - 2U_{AB}(R^0_{nm}). \tag{A1}$$

Kanzaki forces:

$$\begin{aligned} \psi^{i}_{nm} = -\{&\bar{c}U'_{BB}(R^0_{nm}) - (1-\bar{c})U'_{AA}(R^0_{nm}) \\ &+(1-2\bar{c})U'_{AB}(R^0_{nm})\}\frac{(R^{0i}_m - R^{0i}_n)}{R^0_{nm}}, \end{aligned} \tag{A2}$$

where the superscript $'$ denotes the derivative with respect to $R_{nm}$.

Dynamical matrix:

$$\phi^{ij}_{nm} = -\delta_{ij}\frac{\tilde{U}'\left(R^0_{nm}\right)}{R^0_{nm}} + \left\{\frac{\tilde{U}'\left(R^0_{nm}\right)}{R^0_{nm}} - \tilde{U}''\left(R^0_{nm}\right)\right\} \times \frac{\left(R^{0i}_m - R^{0i}_n\right)\left(R^{0j}_m - R^{0j}_n\right)}{{R^0_{nm}}^2}, \tag{A3}$$

$$\phi^{ij}_{nn} = \delta_{ij}\sum_{p\neq 0}\frac{\tilde{U}'\left(R^0_{np}\right)}{R^0_{np}} - \sum_{p\neq 0}\left\{\frac{\tilde{U}'\left(R^0_{np}\right)}{R^0_{np}} - \tilde{U}''\left(R^0_{np}\right)\right\} \times \frac{\left(R^{0i}_n - R^{0i}_p\right)\left(R^{0j}_n - R^{0j}_p\right)}{{R^0_{np}}^2}, \tag{A4}$$

where $\tilde{U}(R_{nm})$ corresponds to

$$\tilde{U}(R_{nm}) = \bar{c}^2\, U_{BB}\left(R^0_{nm}\right) + (1-\bar{c})^2\, U_{AA}\left(R^0_{nm}\right) + 2\bar{c}(1-\bar{c})\, U_{AB}\left(R^0_{nm}\right). \tag{A5}$$

## APPENDIX B: DLA FOR FCC BINARY ALLOY

In this appendix, the details of the discrete lattice approach implementation in the case of an fcc lattice with Cauchy relation are given. Cubic crystals have three independent elastic constants. Equation (11), which links elastic constants with a dynamical matrix, can be rewritten with the following set of equations:

$$\begin{aligned} C_{11} &= -\frac{1}{2v_0}\sum_{\mathbf{R}}\phi^{11}(\mathbf{R})R^1R^1,\\ C_{12}+C_{44} &= -\frac{1}{v_0}\sum_{\mathbf{R}}\phi^{12}(\mathbf{R})R^1R^2,\\ C_{44} &= -\frac{1}{2v_0}\sum_{\mathbf{R}}\phi^{11}(\mathbf{R})R^2R^2. \end{aligned} \tag{B1}$$

When limiting the sum over $\mathbf{R}$ to the second nearest neighbors and assuming a pair potential form for the dynamical matrix, this system of equation becomes

$$\begin{aligned} C_{11} &= \frac{4}{a}\left(\alpha_1 - \frac{\beta_1}{2} + \alpha_2 - \beta_2\right),\\ \frac{C_{12}+C_{44}}{2} &= -\frac{\beta_1}{a},\\ C_{44} &= \frac{4}{a}\left(\alpha_1 - \frac{\beta_1}{4} + \alpha_2\right), \end{aligned} \tag{B2}$$

where $\alpha_N$ and $\beta_N$ are defined in Eq. (21). The Cauchy relation imposes

$$\alpha_1 + \alpha_2 = 0. \tag{B3}$$

In order to identify the $\alpha_N$ and $\beta_N$ parameters, we also fix $\alpha_1 = 0$. Finally, the identification of these parameters from macroscopic data is given by

$$\begin{aligned} &\alpha_1 = 0 \quad \text{(Imposed)}, \quad \beta_1 = -aC_{12},\\ &\alpha_2 = 0, \quad \beta_2 = -\frac{a}{4}(C_{11} - 2C_{12}). \end{aligned} \tag{B4}$$

For Kanzaki forces, Eq. (18) adopts the following form:

$$\sum_m \psi^i_{0m} R^j_m = -v_0\epsilon^0_{ij}(C_{11} + 2C_{12}). \tag{B5}$$

Due to the strong short-range character of Kanzaki forces, the sum over $m$ is limited here to the first neighbors. Indeed, when calculating their values exactly from the continuous pair potential, the second-neighbor value is negligible. Therefore we have

$$\delta_1 = -\frac{v_0}{4a}\epsilon^0(C_{11} + 2C_{12}), \tag{B6}$$

where $\delta_1$ is defined in Eq. (22).

---

[*] currently at CEA, DEN/DMN/SRMP, Service de Recherche de Métallurgie Physique, 91191 Gif-sur-Yvette, France; celine.varvenne@cea.fr

[1] A. G. Khatchaturyan, *The Theory of Structural Transformations in Solids* (Wiley, New York, 1983).

[2] G. Boussinot, Y. Le Bouar, and A. Finel, Acta Mater. **58**, 4170 (2010).

[3] Y. Le Bouar, *Influence des Effets Élastiques lors de la Mise en Ordre Cohérente dans le Système Co-Pt.* (Ecole Polytechnique, France, 1998).

[4] H. E. Cook and D. de Fontaine, Acta Mater. **17**, 915 (1969).

[5] M. A. Krivoglaz, *Diffuse Scattering of X-rays and Neutrons by Fluctuations* (Springer, New York, 1996).

[6] A. Baskaran, J. Devita, and P. Smereka, Continuum Mech. Thermodyn. **22**, 1 (2010).

[7] M. Asta and S. M. Foiles, Phys. Rev. B **53**, 2389 (1996).

[8] J. D. Althoff, D. D. Johnson, and F. J. Pinski, Phys. Rev. Lett. **74**, 138 (1995).

[9] O. M. Ivasishin, N. S. Kosenko, S. V. Shevchenko, N. S. Tatarenko, and V. A. Tsynman, Metalophysica Novejshie Technologii **19**, 8 (1997), in Russian.

[10] D. de Fontaine, Solid State Commun. **34**, 73 (1979).

[11] M. S. Daw and R. D. Hatcher, Solid State Commun. **56**, 697 (1985).

[12] A. Gonis, X.-G. Zhang, A. J. Freeman, P. E. A. Turchi, G. M. Stocks, and D. M. C. Nicholson, Phys. Rev. B **36**, 4630 (1987).

[13] M. Fevre, C. Varvenne, A. Finel, and Y. Le Bouar [Philosophical Magazine (to be published)].

[14] I. Braems, J. Creuze, F. Berthier, R. Tetot, and B. Legrand, Surf. Sci. **602**, 1903 (2008).

[15] V. Ozolins, M. Asta, and J. J. Hoyt, Phys. Rev. Lett. **88**, 9 (2002).

[16] P. Fratzl and O. Penrose, Acta Metall. Mater. **43**, 2921 (1995).

[17] P. Fratzl and O. Penrose, Acta Metall. Mater. **44**, 3227 (1996).

[18] C. A. Laberge, P. Fratzl, and J. L. Lebowitz, Acta Mater. **45**, 3949 (1997).

[19] D. R. Trinkle, Phys. Rev. B **78**, 014110 (2008).

[20] N. W. Ashcroft and N. D. Mermin, *Solid State Physics* (Brooks-Cole, Belmont, MA, 1976).

[21] Y. S. Li, Z. Chen, Y. L. Lu, Y. W. Wang, and Q. B. Lai, Mater. Lett. **61**, 974 (2007).

[22] H. Zapolsky, S. Ferry, X. Sauvage, D. Blavette, and L.-Q. Chen, Philos. Mag. **90**, 337 (2010).

[23] H. Zapolsky, X. Sauvage, R. Patte, S. Ferry, D. Blavette, and L.-Q. Chen, Int. Conf. Solid-Solid Phase Transform. Inorg. Mater. **2**, 783 (2005).

[24] Z. W. Lu, D. B. Laks, S.-H. Wei, and A. Zunger, Phys. Rev. B **50**, 6642 (1994).

[25] One Monte Carlo step corresponds to one attempt of atom exchange per atom (or particle) in the simulation box.

[26] A. D. Sequeira, H. A. Calderon, G. Kostorz, and J. S. Pedersen, Acta Metall. Mater. **43**, 3427 (1995).

[27] I. M. Lifshitz and V. V. Slyozov, J. Phys. Chem. Solids **19**, 35 (1961).

[28] C. Wagner, Z. Elektrochem. **65**, 581 (1961).

[29] J. L. Sanchez, F. Ducastelle, and D. Gratias, Physica **30**, 63 (1984).

[30] J. W. D. Connolly and A. R. Williams, Phys. Rev. B **27**, 5169 (1983).

[31] I. B. Ramsteiner, O. Shchyglo, M. Mezger, A. Udyansky, V. N. Bugaev, and S. S. Schoeder, Acta Mater. **56**, 1298 (2008).

[32] F. R. Nabarro, Philos. Mag. **42**, 1224 (1951).

[33] D. Rodney and A. Finel, Mater. Res. Soc. Symp. Proc. **652**, (2001).

[34] D. Rodney and A. Finel, Acta Mater. **51**, 1730 (2003).